Impact of surface rheology on droplet coalescence in uniaxial compressional flow

Natasha Singh* and Vivek Narsimhan†
Davidson School of Chemical Engineering, Purdue University, 480 Stadium Mall Drive, West Lafayette, Indiana 47907, USA

(Received 24 January 2023; accepted 12 July 2023; published 16 August 2023)

In this study, we perform boundary-integral simulations to understand the role of interfacial viscosity on the early stages of coalescence of two equal-sized droplets approaching under uniaxial compressional flow in the Stokes flow limit. We model the surface rheology of the droplet using the Boussinesq-Scriven constitutive relationship for a Newtonian interface. Previous studies have shown that colliding droplets at low capillary numbers $Ca \sim \mathcal{O}(10^{-4})$ (i.e., low impact velocities) remain almost spherical up to the point of film rupture, while droplets at large values of capillary number form a dimpled film that significantly slows down the drainage time. Here we explore how the interfacial viscosity affects the thin film formation and drainage time in a head-on collision between two droplets with capillary number values in the range $10^{-4}-10^{-2}$. We observe that the surface viscosity significantly arrests the thinning of the film between the coalescing droplets compared to a clean interface. We find that the film drainage time at a given capillary number increases upon increasing the Boussinesq parameter for total surface viscosity and is independent of the ratio of surface dilatational viscosity to the surface shear viscosity. We also explore the coupled influence of surface viscosity and Marangoni stresses on droplet coalescence. We incorporate the effect of surfactant transport by solving the time-dependent convection-diffusion equation and consider a nonlinear equation of state (Langmuir adsorption isotherm) to correlate the interfacial tension with the changes in surfactant concentration.

DOI: 10.1103/PhysRevFluids.8.083602

I. INTRODUCTION

Understanding how interfacial rheology, i.e., the elastic and viscous resistances of the interface, alters droplet coalescence and breakup plays an essential role in understanding how complex foams/emulsions are created and stabilized. Complex interfacial interactions in droplet coalescence and breakup influence the dynamics of various industrial applications like inkjet printing, spraying systems, fuel/water separations, stabilization of food emulsions, drug formulation, and drug encapsulation [1–9]. Droplet breakup occurs above a critical external flow velocity or capillary number value. On the contrary, coalescence is favored by gentle collisions between two droplets, i.e., weak flows or small capillary numbers [10–12]. The external flow governs the total collision time for coalescence, and the total collision time decreases upon increasing the capillary number. On the other hand, the film's drainage time increases upon increasing the capillary number. Under weak flows, collisions are long enough to allow the thin film to drain and eventually rupture. Therefore, a critical capillary number exists beyond which no coalescence is observed for two colliding droplets.

*singh567@purdue.edu
†vnarsim@purdue.edu

The flow-induced coalescence between two droplets occurs in three sequential stages: (a) approach of droplets under external flow, (b) formation of thin film between the two droplets and subsequent drainage, and (c) rupture of thin film, at which point the droplets are close enough for the destabilizing van der Waals force across the film to overcome the stabilizing interfacial tension force. The first stage is characterized by the properties of the external flow [10]. Several factors can influence the formation and drainage of the film: the ratio of the drop fluid viscosity to the suspending fluid viscosity, external flow rate, droplet radius, surfactant concentration, surfactant mobility on the interface, surfactant solubility in the drop and suspending fluid, surface tension, and interfacial stresses due to Marangoni effects and surface rheology. Depending on these factors, the mobility of the thin film can be classified as immobile, partially mobile, or fully mobile [10,13]. The theoretical scaling of the film thickness with drainage time, assuming either a flat film approximation or lubrication model, has been developed in many studies in the limiting situations of immobile, partially mobile, and fully mobile surfaces for clean droplets and droplets covered with simple surfactants [10,12–18].

For flow-induced head-on collision between two equal-sized clean droplets at very low capillary numbers, studies have shown that the droplet shape remains almost spherical up to the point of film rupture [11,12]. The total time for the film to drain, scaled by the external flow extension rate, has been reported to be independent of the droplet size [11,12]. However, as the capillary number increases $Ca \geqslant \mathcal{O}(10^{-3})$, the droplet forms a more deformed film, and at a sufficiently large capillary number, the film develops a dimpled shape [11]. The total time for the film to drain increases upon increasing the capillary number. Numerical simulations to model the full coalescence process from collision to the point where the film approaches rupture using the boundary element method are developed by [11,19,20]. The numerical results of axisymmetric boundary integral simulations for clean droplet coalescence from [11] were reported to be in good quantitative agreement with the experimental results from [12] for polybutadiene drops suspended in polydimethylsiloxane. It is well known that the adsorption of simple surfactants on the droplet interface inhibits or slows down the coalescence process due to Marangoni stresses [21–25]. As the film drains, the surfactant is swept toward the film edges, which gives rise to nonhomogenous surfactant distribution. Resultant surface tension gradients over the thin film oppose the film drainage and enhance the dimpling of the film compared to a clean droplet at the same value of the capillary number. Axisymmetric boundary element simulations to model the effect of surfactant transport on droplet coalescence are developed by [24,25]. An extensive review of the effect of surfactants on droplet coalescence using numerical and various experimental techniques at the macroscale and microscale is provided by [26].

Surface rheology plays an essential role in droplet dynamics for interfaces embedded with a monolayer of proteins, lipid bilayers, polymers, and solid particulates [27–34]. The effect of surface rheology on droplet coalescence remains underexplored. In the case of certain alcohols, lipids, and proteins adsorbed onto a droplet, the droplet forms a predominantly viscous interface [28,35–37]. The resulting interfacial stresses for such surfactant surfaces can be modeled using the Boussinesq-Scriven equation. In this work, we examine the interplay of surface shear and dilatational viscosity and surfactant transport on the dynamics of droplet coalescence under head-on collision using boundary-element simulation.

II. PROBLEM SETUP AND METHODOLOGY

A. Problem statement

Figure 1 shows the schematic of the problem statement. We model the coalescence of two equal-sized droplets approaching under axisymmetric compressional flow in the Stokes flow limit. The undisturbed external flow field $\boldsymbol{u}'_\infty$ is given by the expression

$$\boldsymbol{u}'_\infty = \frac{G'}{2} \cdot \begin{bmatrix} -2 & 0 & 0 \\ 0 & 1 & 0 \\ 0 & 0 & 1 \end{bmatrix} \cdot \boldsymbol{x}', \tag{1}$$

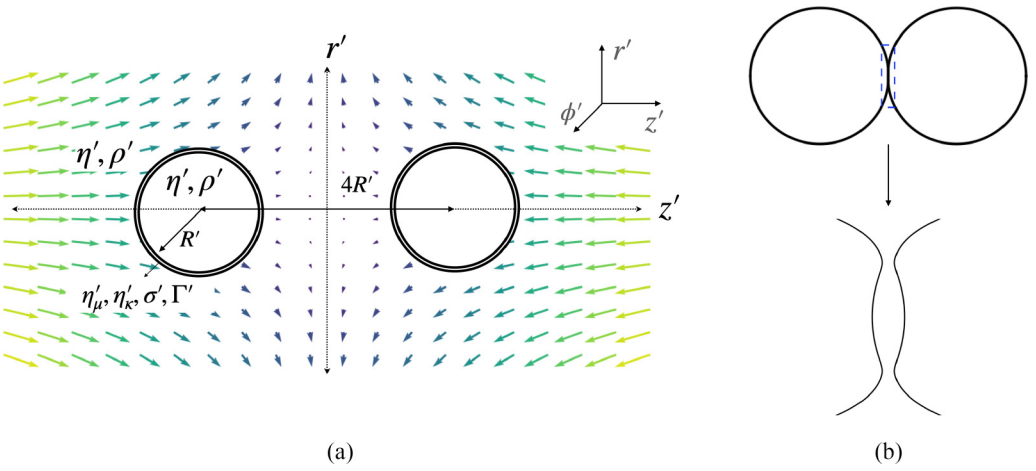

(a) (b)

FIG. 1. (a) Problem overview, (b) Zoomed-in image of the thin film formed between the two droplets as they coalesce under external flow.

where G' represents the external extension rate, and $\boldsymbol{x'} = [\, z',\ r'\cos\phi',\ r'\sin\phi'\,]$ represents the position vector. All quantities are expressed in polar cylindrical coordinates (z', r', ϕ') and the system is axisymmetric about the z' -axis. We assume both the drop and suspending fluid have equal fluid viscosity η' and density ρ'. Initially, the shapes of the two droplets are spherical with an undeformed radius R'. At time $t' = 0$, the droplets are placed at a separation of $4R'$ measured from the center of one droplet to another, as shown in Fig. 1. The interface of the droplet is covered with a viscous insoluble monolayer of surfactant. The surface rheology of the viscous interface is modeled using the Boussinesq-Scriven constitutive relationship for a Newtonian interface [38,39]. The interface has a surface shear viscosity η'_μ and a surface dilatational viscosity η'_κ. Quantities σ' and Γ' represent the local surface tension and the local surfactant concentration on the interface, respectively. Figure 1(b) shows the zoomed-in image of the thin film that is formed between the two droplets as they coalesce under the external flow. The objective of this study is to understand how interfacial rheology alters the shape and drainage time of this thin liquid film.

B. Nondimensionalization

We nondimensionalize all lengths by radius R', viscosities by η', times by G'^{-1}, velocities by $G'R'$, bulk stresses by $\eta'G'$, surface stresses by $R'\eta'G'$, surface tension by its equilibrium value σ'_{eq}, and surface concentration by Γ'_{eq}. Throughout the manuscript, primed variables are in dimensional form, and unprimed variables are in dimensionless form.

C. Governing equations

The fluid flow in the drop and the suspending fluid is governed by the Stokes and continuity equations. Stokes and continuity equations in the dimensionless form are given below:

$$\lambda\nabla^2\boldsymbol{u}^d = \nabla p^d, \quad \nabla\cdot\boldsymbol{u}^d = 0, \tag{2a}$$

$$\nabla^2\boldsymbol{u}^c = \nabla p^c, \quad \nabla\cdot\boldsymbol{u}^c = 0. \tag{2b}$$

In the above equations, the quantities in the drop phase have a superscript d, and the quantities in the suspending phase have a superscript c. The viscosity ratio of the drop fluid to the suspending fluid is $\lambda = 1$. At the droplet interface, the boundary conditions are

(i) Continuity of velocity

$$\boldsymbol{u^d} = \boldsymbol{u^c} = \boldsymbol{u_s}, \tag{3}$$

where $\boldsymbol{u_s}$ is the velocity of the droplet interface.

(ii) Traction balance in dimensionless form

$$(\boldsymbol{\tau}^c - \boldsymbol{\tau}^d) \cdot \boldsymbol{n} = \boldsymbol{f_\mu} + \boldsymbol{f_\kappa} + \frac{1}{Ca}(\sigma \boldsymbol{n} \nabla \cdot \boldsymbol{n} - \nabla_s \sigma) - \frac{A}{Ca\, h^3}\boldsymbol{n}. \tag{4}$$

In the above equation, $\boldsymbol{\tau}^c - \boldsymbol{\tau}^d$ is the traction jump across the interface, $\boldsymbol{f_\mu}$ is the interfacial shear traction, and $\boldsymbol{f_\kappa}$ is the interfacial dilatational traction. The last two terms on the left side of Eq. 4 denote the traction contribution from variable surface tension and attractive van der Waals force, respectively. $Ca = G'\eta' R'/\sigma'_{\text{eq}}$ represents the capillary number, σ is the dimensionless surface tension, $\boldsymbol{n}$ is the outward pointing normal, $\nabla_s = \boldsymbol{P} \cdot \nabla$ is the surface gradient ($\boldsymbol{P} = \boldsymbol{I} - \boldsymbol{nn}$ is the projection operator on the surface), $A = \frac{A_h}{6\pi R'^2 \sigma'_{\text{eq}}}$ is the dimensionless Hamaker constant, and h is the local film thickness.

The expressions for the interfacial shear traction $\boldsymbol{f_\mu}$ and the interfacial dilatational traction $\boldsymbol{f_\kappa}$ are given by the Boussinesq-Scriven constitutive relationship [38,39]:

$$\boldsymbol{f_\kappa} = -\nabla_s \cdot [Bq_\kappa \boldsymbol{P}(\nabla_s \cdot \boldsymbol{u_s})], \tag{5}$$

$$\boldsymbol{f_\mu} = \nabla_s \cdot Bq_\mu \big[\boldsymbol{P}(\nabla_s \cdot \boldsymbol{u_s}) - \boldsymbol{P} \cdot \left(\nabla_s \boldsymbol{u_s} + \nabla_s \boldsymbol{u_s}^T\right) \cdot \boldsymbol{P}\big]. \tag{6}$$

$Bq_\mu = \frac{\eta'_\mu}{R'\eta'}$ is the Boussinesq number for the surface shear viscosity, and $Bq_\kappa = \frac{\eta'_\kappa}{R'\eta'}$ is the Boussinesq number for the surface dilatational viscosity. $Bq = Bq_\mu + Bq_\kappa$ is the total Boussinesq number representing the ratio of the interfacial viscous forces to the bulk viscous forces. We define $\lambda_{ds} = \eta'_\kappa/\eta'_\mu$ as the ratio of surface dilatational viscosity to the surface shear viscosity.

The evolution of surfactant concentration Γ on the interface with time is modeled using the time-dependent convection-diffusion equation [40,41]:

$$\frac{\partial \Gamma}{\partial t} + \nabla_s \cdot (\Gamma \boldsymbol{u_t}) + \Gamma(\nabla_s \cdot \boldsymbol{n})(\boldsymbol{u_s} \cdot \boldsymbol{n}) = \frac{1}{Pe_s}\nabla_s^2 \Gamma. \tag{7}$$

In the above equation, $\boldsymbol{u_t} = \boldsymbol{u_s} - \boldsymbol{n}(\boldsymbol{u_s} \cdot \boldsymbol{n})$ is the tangential component of the interfacial velocity, $Pe_s = \frac{G'R'^2}{D'_s}$ is the surface Peclet number, and D'_s is the interface diffusivity of the surfactant.

We assume a nonlinear Langmuir equation of state to relate the surface tension to surfactant concentration on the interface at any point. The Langmuir equation in dimensionless form is

$$\sigma = \frac{\sigma'_o}{\sigma'_{\text{eq}}} + \frac{R'_G T' \Gamma'_\infty}{\sigma'_{\text{eq}}} \ln\left(1 - \frac{\Gamma}{\Gamma_\infty}\right), \tag{8}$$

where, $\sigma = \frac{\sigma'}{\sigma'_{\text{eq}}}$, $\Gamma = \frac{\Gamma'}{\Gamma'_{\text{eq}}}$, R'_G is the ideal gas constant, T' is the absolute temperature, Γ'_∞ is the maximum packing density for a given surfactant system, and $\Gamma_\infty = \frac{\Gamma'_\infty}{\Gamma'_{\text{eq}}}$.

The equilibrium surface tension σ'_{eq} can be related to the equilibrium surfactant concentration Γ'_{eq} as follows:

$$1 = \frac{\sigma'_o}{\sigma'_{\text{eq}}} + \frac{R'_G T' \Gamma'_\infty}{\sigma'_{\text{eq}}} \ln\left(1 - \frac{\Gamma'_{\text{eq}}}{\Gamma'_\infty}\right). \tag{9}$$

Upon subtracting Eq. (9) from Eq. (8), we get

$$\sigma = 1 + E \ln\left(\frac{\Gamma_\infty - \Gamma}{\Gamma_\infty - 1}\right), \tag{10}$$

TABLE I. Dimensionless parameters.

Ca	Capillary number	$Ca = \frac{G'\eta' R'}{\sigma'_{eq}}$	$10^{-4} \leqslant Ca \leqslant 10^{-2}$
Bq_μ	Boussinesq parameter for surface shear viscosity	$Bq_\mu = \frac{\eta'_\mu}{R'\eta'}$	$0 \leqslant Bq_\mu \leqslant 2$
Bq_κ	Boussinesq parameter for surface dilatational viscosity	$Bq_\kappa = \frac{\eta'_\kappa}{R'\eta'}$	$0 \leqslant Bq_\kappa \leqslant 2$
Bq	Boussinesq parameter for total surface viscosity	$Bq = \frac{\eta'_\kappa + \eta'_\mu}{R'\eta'}$	$0 \leqslant Bq \leqslant 2$
Pe_s	Surface Peclet number	$Pe_s = \frac{CaR'\sigma'_{eq}}{D'_s\eta'}$	$Pe_s = 25.7 \times 10^3 \times Ca$
E	Surface elasticity number	$E = \frac{R'_G T' \Gamma'_\infty}{\sigma'_{eq}}$	$E = 0.25$
Γ_∞	Initial surfactant coverage	$\Gamma_\infty = \frac{\Gamma'_\infty}{\Gamma'_{eq}}$	$\Gamma_\infty = 24.5$

where $E = \frac{R'_G T' \Gamma'_\infty}{\sigma'_{eq}}$ is the surface elasticity number. Using the above equation, the traction contribution from surface tension in Eq. (4) can be written as

$$\frac{1}{Ca}(\sigma \boldsymbol{n}\nabla\cdot\boldsymbol{n} - \nabla_s\sigma) = \frac{1}{Ca}\left(\boldsymbol{n}\nabla\cdot\boldsymbol{n} + E\ln\frac{\Gamma_\infty - \Gamma}{\Gamma_\infty - 1}\boldsymbol{n}\nabla\cdot\boldsymbol{n} + \frac{E}{\Gamma_\infty - \Gamma}\nabla_s\Gamma\right). \tag{11}$$

The surface shear and dilatational viscosity can depend greatly on surface pressure $\Pi' = \sigma'_c - \sigma'$ [27,36,42–44]. To incorporate the effect of pressure-dependent surface viscosity, we describe the Boussinesq numbers for pressure thickening/thinning surface shear and dilatational viscosity as

$$Bq^{\pm}_\mu = Bq_{\mu,eq}\, e^{\pm\frac{1-\sigma}{\Pi_c}}, \tag{12}$$

$$Bq^{\pm}_\kappa = Bq_{\kappa,eq}\, e^{\pm\frac{1-\sigma}{\Pi_c}}. \tag{13}$$

In the above equations, a positive sign indicates a pressure-thickening surfactant, while a negative sign indicates a pressure-thinning surfactant. Quantity Π_c denotes the dimensionless surface pressure scale.

D. Dimensionless parameters and typical experimental values

Table I summarizes the characteristic dimensionless parameters in this study. Since the coalescence between two droplets is facilitated by slow, gentle collisions, we look at capillary number values in the range 10^{-4}–10^{-2}. The experimentally measured value of surface shear viscosity η'_μ for different viscous interfaces (for instance: eicosanol, hexadecanol, sodium dodecyl sulfate, β–casein, and POPC) generally lies in the range $(10^{-6}$–$10^{-2})$ $N\cdot s/m$ [27,28,37,45–49]. Also, the ratio of surface shear to dilatational viscosity $\lambda_{ds} = \frac{\eta'_\kappa}{\eta'_\mu}$ is found to be very large $\lambda_{ds} \sim \mathcal{O}(1 - 10^6)$ for many lipids, proteins, and fatty alcohols [35,42,43,50–54]. Assuming suspending fluid viscosity η' varies in the range (10^{-3}–10 Ns/m^2) and droplet radius R' in the range (10–1000 μm), the value of Boussinesq number Bq can vary in the range $\mathcal{O}(10^{-4}-10^6)$. In this study, we consider values of total Boussinesq number $Bq = Bq_\mu + Bq_\kappa \sim \mathcal{O}(1)$ and interfacial viscosity ratio λ_{ds} values in the range $0 \leqslant \lambda_{ds} \leqslant \infty$.

The typical value of compression rate G' in experiments is found to be $G' \sim O(1)$ s^{-1} [55]. The surfactant diffusivity D'_s is found to vary in the range $D'_s \sim \mathcal{O}(10^{-14}$–$10^{-8})$ m^2/s for different materials [56]. Assuming droplet radius R' in the range (10–1000 μm), the surface Peclet number can vary in the range $(10^{-2}-10^8)$. For different materials, experimental value of surface elasticity $E = \frac{R'_G T' \Gamma'_\infty}{\sigma'_{eq}}$ is found to be of $\mathcal{O}(10^{-1})$ [27,28,35,37,43,45,47–49,57,58]. In this work, for surfactant transport parameters, we take the values from previous experimental and computational studies

on droplet coalescence that considered a system of polybutadiene (PBd) droplets suspended in polydimethylsiloxane (PDMS) with insoluble block copolymer on the interface [11,24]. For the PBd-PDMS-PBd droplet system studied in [24], the value of Hamaker constant is 3.2×10^{-21} J, the radius of the initially spherical droplet is 27 μm, the quantity $R'_G T' \Gamma'_\infty = 1.2$ mN /m, the surface diffusivity of surfactant is 1.7×10^{-9} cm^2/s, the surface tension of clean interface is $\sigma'_o = 4.8$ mN/m, the viscosity of the suspending fluid PDMS is 29.3 $Pa \cdot s$. For the simulations shown in this study, we assume the equilibrium surface tension in the presence of surfactants to be $\sigma'_{\text{eq}} = 4.75$ mN/m. Upon substituting the above values in the dimensionless parameters, we get initial surfactant coverage $\Gamma_\infty = 24.5$, surface elasticity number $E = 0.25$, and surface Peclet number $Pe_s = 25.7 \times 10^3 \times Ca$.

We lastly make a general comment on when surface rheology would be important compared to Marangoni effects. The relative magnitude of the Marangoni effects to surface viscous effects $\frac{Ma}{Bq} = \frac{Pe_s E}{Ca\, Bq}$ tells when one effect is more important than another. For capillary number $Ca = \mathcal{O}(10^{-3})$, surface diffusivity $D_s = \mathcal{O}(10^{-10})$ m^2/s, elasticity $E = \mathcal{O}(10^{-1})$, and Boussinesq number $Bq = \mathcal{O}(1)$, $\frac{Ma}{Bq} = R'^2 * 10^{12}$. Thus, if surface rheology were present, it would become important for droplets in nano and microemulsions ($R' = 10^{-8} - 10^{-6} m$) and less important for millimeter-sized droplets ($R' = 10^{-3}$ m).

E. Numerical implementation

We discretize each droplet's interface into a set of N connecting nodes. The velocity of a node at interfacial location $\boldsymbol{x_o}$ is numerically computed using the axisymmetric boundary-integral equation [59,60]:

$$\boldsymbol{u_s}(\boldsymbol{x_0}) = \boldsymbol{u_\infty}(\boldsymbol{x_0}) - \frac{1}{8\pi} \int_{C_1+C_2} \boldsymbol{M}(\boldsymbol{x}, \boldsymbol{x_0}) \cdot [[\boldsymbol{\tau} \cdot \boldsymbol{n}]]\, dl(\boldsymbol{x}). \tag{14}$$

In the above equation, $\boldsymbol{u_\infty}(\boldsymbol{x_0})$ is the contribution from applied flow field. The second term on the right-hand side of the equation denotes the single-layer potential, where $\boldsymbol{M}$ is the axisymmetric free space Green's function [59,60], $[[\boldsymbol{\tau} \cdot \boldsymbol{n}]] = (\boldsymbol{\tau}^c - \boldsymbol{\tau}^d) \cdot \boldsymbol{n}$ is the traction jump across the interface, and dl is the differential arc length along the droplet interface. The integral is carried out along the contour of both droplets ($C_1 + C_2$). Because of the symmetry of the problem about the r' axis, we carry out all the computations on one droplet.

We represent the position and velocity vector at any interfacial location on the droplet using cubic spline interpolation parametrized in terms of the cumulative polygonal arclength s. The numerical details on spline parametrization of position and velocity vectors and on computation of single layer line integral in Eq. (14) can be found in [61].

At $t = 0$, the center-to-center distance between the two droplets is $4R'$, and the shapes are spherical. The surfactant concentration is initially assumed to be uniformly distributed over the droplet's interface. We consider cubic spline parametrization for surfactant concentration on the droplet's interface similar to the position vector and at $t = 0$, $\Gamma = 1$ at the N node locations. The simulations at $t = 0$ are started using $N = 100$ mesh points on each droplet's interface.

We perform the following procedure to obtain the evolution of droplet shapes with time:

(i) **Compute velocity:** At the time t, given the droplet shape and surfactant concentration values, the velocity vector is computed using the boundary integral equation (14).

(ii) **Update droplet shape:** The updated droplet shape at time $t + \Delta t$ is obtained by advancing the nodes on the droplet interface using the explicit Euler method.

(iii) **Remeshing:** A node is inserted between the two nodes using cubic spline interpolation if (a) the distance between two mesh points becomes large $\Delta d > \frac{1.3\pi}{N}$ or (b) the distance between two mesh points is greater than the local film thickness $\Delta d > h$.

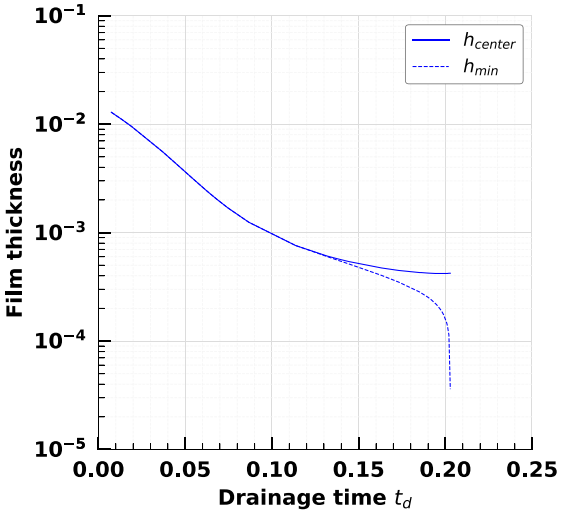

FIG. 2. Evolution of film thickness $h_{\min}$ and h_{center} with drainage time t_d for a clean droplet at $Ca = 0.001$ ($Bq = 0, E = 0$).

Similarly, we remove one of the nodes if (a) away from the thin film region, the distance between two mesh points becomes too small, i.e., $\Delta d < \frac{0.16\pi}{N}$ or (b) in the thin film region, the distance becomes too small compared to local film thickness $\Delta d < (0.4 \times h)$.

(iv) **Update surfactant concentration:** The surfactant concentration is updated using the implicit Euler method. The numerical procedure to solve the convection-diffusion equation using cubic splines is similar to that described in [61].

We rescale the node's position and surfactant concentration after each time step to conserve the droplet volume and total surfactant on the droplet's interface.

The initial time step Δt_s in simulations where surfactant transport effects are neglected is set to $\Delta t_s = 0.01 \cdot Ca$. In the presence of surfactant transport effects, the initial time step is set to $\Delta t_s = 0.005 \cdot Ca$. As the film between the two droplets begins to drain, the time step is further reduced to maintain numerical accuracy. In both cases (with and without surfactant transport effects), when the minimum element size in the mesh $\Delta d_{\min} < 0.01$, the time step after each iteration is modified using the relation $\Delta t = (\Delta d_{\min}/0.01) \times \Delta t_s$.

The computational cost of a typical numerical simulation at $Ca = 0.001$ and $Bq = 0.1$ for a droplet without surfactant transport is roughly 500 CPU hours with 64 MPI cores. The computational cost increases as the capillary number, total Boussinesq number, surface elasticity, or surface Peclect number increases.

F. Film drainage

In this manuscript, we define t_o as the start of the drainage process, which is the time when the center-to-center distance between the two droplets is $2 \times R'$. The drainage time $t_d = t - t_o$ is the time elapsed from t_o, while the total film drainage time $T_d = t_c - t_o$ is the time between film rupture (t_c, defined below) and the start of drainage (t_o).

In Fig. 2, we plot the minimum film thickness ($h_{\min}$) and the film thickness along the line of droplet centers (h_{center}) as a function of drainage time (t_d) for a clean droplet without surfactant at $Ca = 0.001$. As shown in Fig. 2, $h_{\min}$ drops dramatically from 10^{-4} to 10^{-5} with drainage time as the film approaches rupture. For the simulation results presented in this manuscript, we approximate the total time for the film drainage T_d by the drainage time t_d at which the minimum film thickness is in the range $h_{\min} \sim (10^{-5}$–$10^{-4})$.

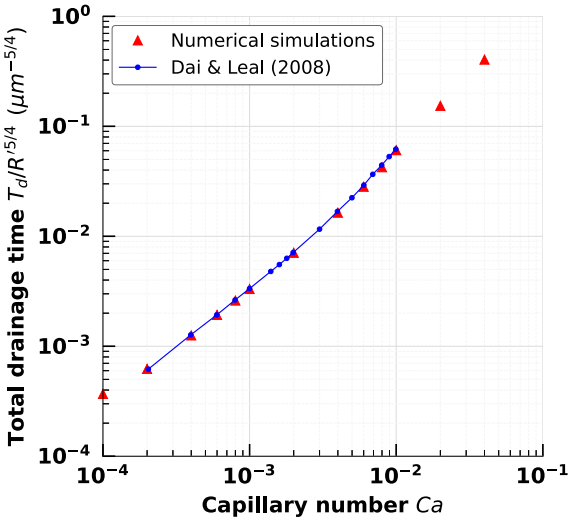

FIG. 3. Total drainage time scaled by droplet radius ($T_d/R'^{5/4}$ μm$^{-5/4}$) as a function of capillary number Ca for a clean droplet system ($Bq = 0$, $E = 0$). The red triangles represent our numerical results, and the blue curve represents the boundary element simulation results from [11,24].

III. RESULTS

A. Validation

To validate the accuracy of our code, we compare our numerical results with boundary element simulation results from previous studies investigating clean droplet coalescence [11,24] and the effect of surfactant transport on droplet coalescence [24].

Figure 3 shows how the total drainage time scaled by droplet radius ($T_d/R'^{5/4}$ μm $^{-5/4}$) changes with the capillary number Ca for clean droplet coalescence. The red triangles represent our numerical results, and the blue curve represents the boundary element simulation results from [11,24]. We see that our results compare well with previous literature. In Fig. 4, we show how the thin film profiles evolve with drainage time for clean droplet coalescence at $Ca = 0.001$. The normalized arclength is $s = 0$ at the center of the thin film and $s = 1$ at the rear end of the droplet. Figure 5 shows the film profiles for coalescence in the presence of surfactant transport with $\sigma'_{\rm eq} = 4.75$ mN /m and $Ca = 0.001$ ($E = 0.25$, $Pe_s = 25.7$). In Figs. 4 and 5, we benchmark our simulation results (shown by black solid curves) against boundary element simulations from [24] (shown by red dashed curves). At the same value of capillary number $Ca = 0.001$, we can see that surfactant transport increases the drainage time compared to a clean droplet. This increase in drainage time can be attributed to the enhanced dimpling effect that arises due to the Marangoni stresses within the thin film for a droplet with surfactant transport [24].

In this study, we assume that at time $t = 0^-$ when the droplets are at a separation of $4R'$, the surfactant is uniformly distributed over the droplet's interface with equilibrium surface tension $\sigma'_{\rm eq}$ and equilibrium surfactant concentration $\Gamma'_{\rm eq}$. We note that even if the simulation is started with a higher initial separation of $16R'$ (measured from the center of one droplet to another) instead of $4R'$, by the time the droplet system is at a separation of $2R'$ (i.e., when drainage starts $t_d = 0$), the surfactant concentration distribution is similar in the two cases (with separation $16R'$ and $4R'$) at $t_d = 0$. The assumption of uniform surfactant concentration at $t = 0$ does not impact the drainage time calculations as the drainage time is found to be independent of the initial separation for distances greater than $4R'$.

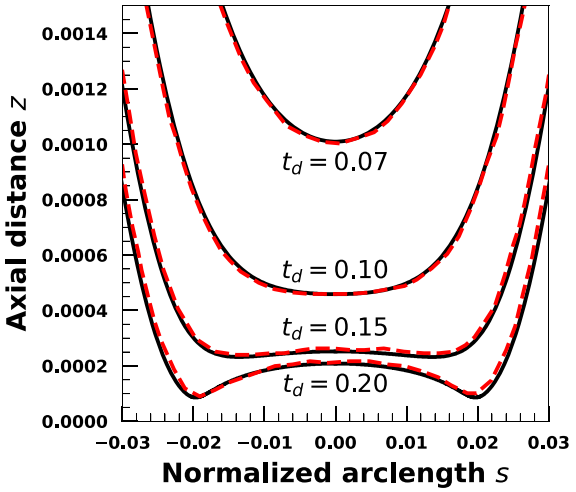

FIG. 4. Film drainage profiles for clean droplet coalescence. The dimensionless parameters are $Ca = 0.001$, $Bq = 0$, and $E = 0$. The black solid curves represent our numerical results, and the red dashed curves represent boundary element simulation results from [24].

B. Results: Droplet with constant surface viscosity and without Marangoni flows

In this section, we look at the role of interfacial viscosity on droplet coalescence. We assume the surface tension remains constant and that the surfactant is homogeneously distributed on the interface ($E = 0$). The first subsection (III B 1) will discuss the individual role of surface shear and dilatational viscosity on the coalescence dynamics, while the next subsection (III B 2) will discuss how the effects of surface viscosity change with capillary number. The combined impact of surface viscosity and Marangoni stresses will be considered later in the manuscript (Sec. III C).

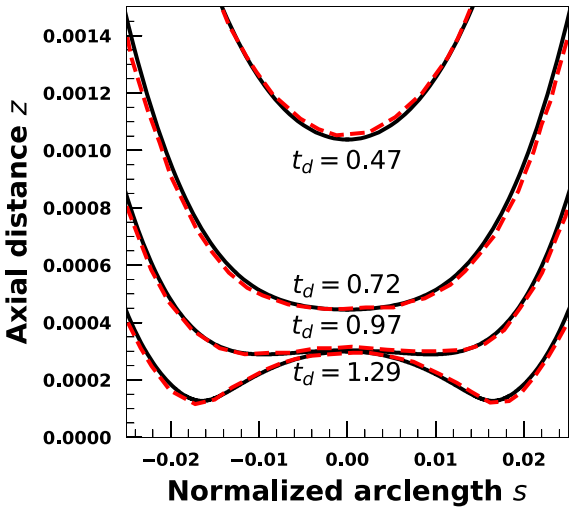

FIG. 5. Film drainage profiles in the presence of surfactant transport. The dimensionless parameters are $Ca = 0.001$, $Bq = 0$, $E = 0.25$, and $Pe_s = 25.7$. The black solid curves represent our numerical results, and the red dashed curves represent boundary element simulation results from [24].

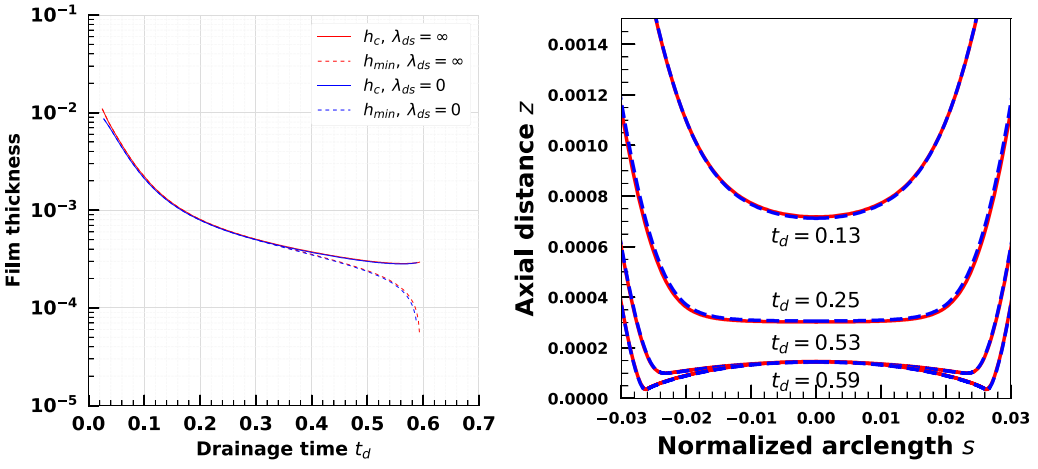

(a) (b)

FIG. 6. Evolution of (a) film thickness ($h_{\min}$ and h_{center}) and (b) film drainage profiles with drainage time (t_d) at $Ca = 0.001$ and $Bq = 0.1$. For (b), blue dotted curves represent results for a droplet with only surface shear viscosity ($\lambda_{ds} = 0$), and red solid curves represent results for a droplet with only surface dilatational viscosity ($\lambda_{ds} = \infty$).

1. Individual role of constant surface shear and dilatational viscosity

Figures 6(a) and 6(b) show the time evolution of (a) film thicknesses ($h_{\min}$ and h_{center}) and (b) film shapes at $Ca = 0.001$ for a droplet with only surface shear viscosity $Bq = 0.1$, $\lambda_{ds} = 0$ (shown by blue curves) and a droplet with only surface dilatational viscosity $Bq = 0.1$, $\lambda_{ds} = \infty$ (shown by red curves). Interestingly, we observe that the results for these two cases overlap—in other words, the results appear to depend only on the sum $Bq = Bq_\mu + Bq_\kappa$ rather than the ratio $\lambda_{ds} = \frac{\eta'_\kappa}{\eta'_\mu}$. To understand this phenomenon, let us look at the lubrication equation for a perfectly planar Newtonian thin film. The stress balance equation at the interface in dimensionless form can be written as [62]

$$\frac{\partial u_r^d}{\partial z} = \frac{\partial u_r^c}{\partial z} + \frac{1}{Ca}\frac{\partial \sigma}{\partial r} + (Bq_\mu + Bq_\kappa)\frac{\partial}{\partial r}\left[\frac{1}{r}\frac{\partial (r u_{s,r})}{\partial r}\right]. \tag{15}$$

In the above equation, u_r^d, u_r^c, and $u_{s,r}$ are the radial components of the velocity in the drop phase, suspending phase, and at the droplet interface, respectively. The lubrication approximation in the thin film also suggests that the coalescence dynamics of a droplet with surface viscosity depend on the sum of shear and dilatational Boussinesq numbers Bq. We find that even for cases when the film is not perfectly planar (e.g., dimpled), this basic observation does not change appreciably. From here on out, we will show results as a function of $Bq = Bq_\kappa + Bq_\mu$, assuming a value of $\lambda_{ds} = 1$ unless otherwise stated.

2. Effect of Ca and Bq

This section discusses the role of Ca and Bq on coalescence dynamics. We will start with observations at a very low capillary number ($Ca = 0.0002$) and then march toward a large capillary number ($Ca = 0.05$). Figure 7 shows the evolution of droplet film shapes as a function of drainage time at a very low capillary number ($Ca = 0.0002$). Three cases are considered: (a) a clean droplet ($Bq = 0$), (b) a droplet with $Bq = 0.2$, and (c) a droplet with $Bq = 2.0$. When the capillary number is as small as is described here, a clean droplet is almost spherical as it drains, and the film eventually ruptures at the center of the droplet. The effect of interfacial viscosity is to widen the film and slow

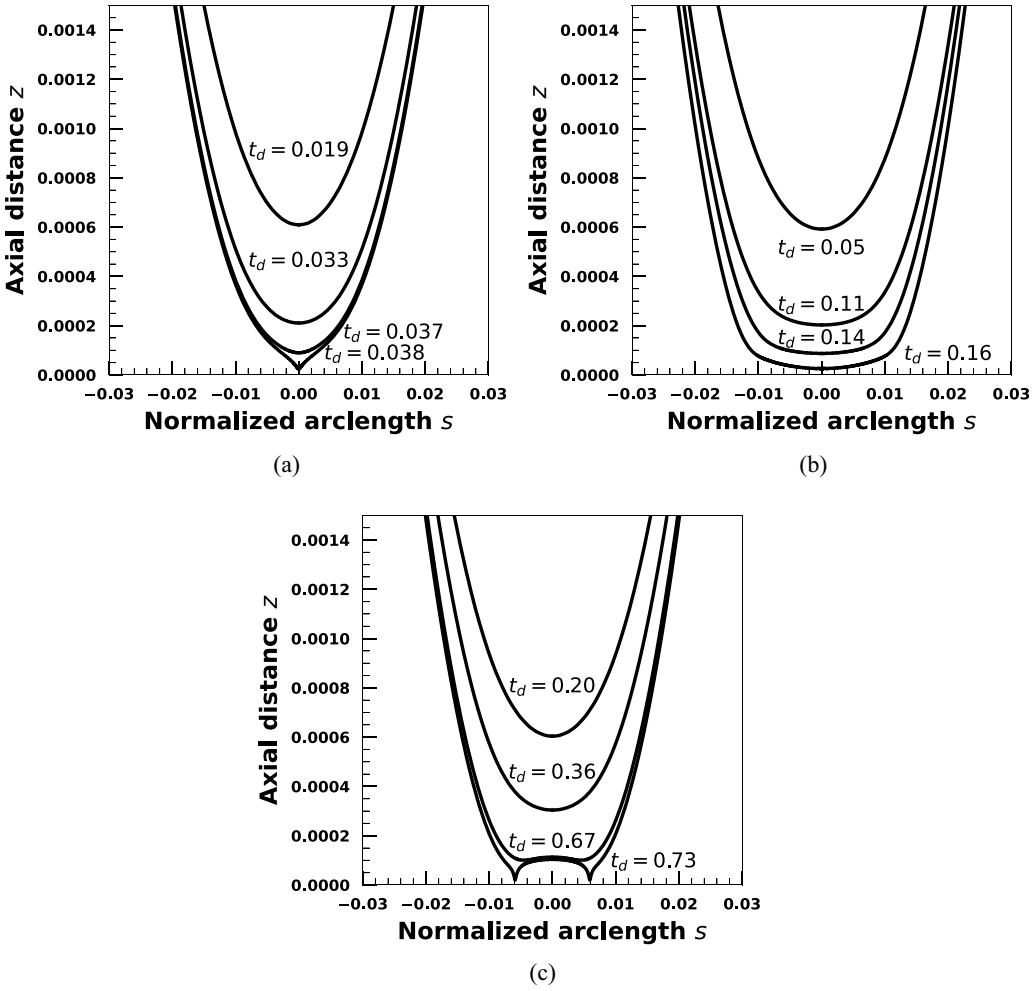

FIG. 7. Film drainage profiles for a clean droplet and droplets with surface viscosity at capillary number $Ca = 0.0002$. (a) Clean droplet ($Bq = 0$), (b) Droplet with surface viscosity: $Bq = 0.2$, $\lambda_{ds} = 1$, and (c) Droplet with surface viscosity: $Bq = 2.0$, $\lambda_{ds} = 1$.

the drainage time compared to a clean droplet. For the droplet with $Bq = 2.0$, the film is widened enough to rupture at the film edges rather than the center. Thus, at low capillary numbers, interfacial viscosity can alter the rupture point for coalescence. Figure 8 plots the increase in total film drainage time T_d upon increasing the total Boussinesq number Bq at capillary number $Ca = 0.0002$. Even a small increase in Bq from 0 to 0.1 increases the total drainage time by 170% with respect to the clean droplet.

At a moderate capillary number value $Ca = 0.001$, we observe that a clean droplet forms a dimple during its drainage process and ruptures at the film edges [Fig. 9(a)]. When interfacial viscosity is added, we observe that rupture also occurs at the film edges, but dimpling is much less pronounced with a wider and flatter film than the clean droplet case [Figs. 9(b) and 9(c)]. The drainage time also increases considerably. For example, upon increasing Bq from 0 to 0.2, we observe that the total drainage time rises from 0.20 to 0.93. We note that this behavior is very different from what occurs with Marangoni stresses, which typically stabilize the film by increasing

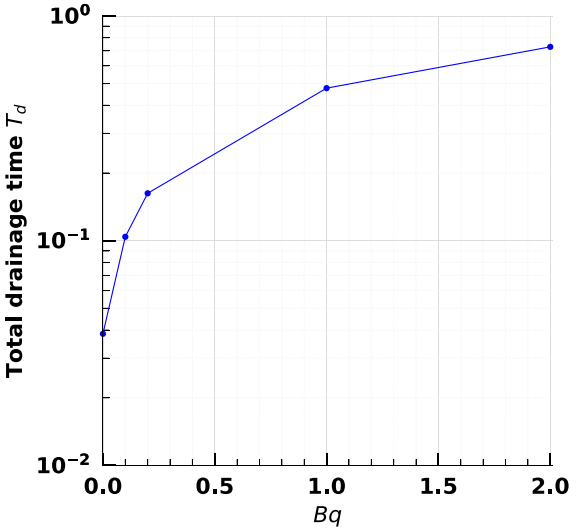

FIG. 8. Total film drainage time T_d as a function of Boussinesq number $Bq = Bq_\mu + Bq_\kappa$ at capillary number value $Ca = 0.0002$.

the dimpling rather than widening the film. To understand this process in more detail, we plot the tractions and velocities at the interface.

In Figs. 10(a) and 10(b), we show how the normal and tangential components of the interfacial viscosity traction [i.e., $(\boldsymbol{f_\mu} + \boldsymbol{f_\kappa}) \cdot \boldsymbol{n}$ and $(\boldsymbol{f_\mu} + \boldsymbol{f_\kappa}) \cdot \boldsymbol{t}$] vary along the thin film for the droplet shape shown in Fig. 9(b) at drainage time $t_d = 0.25$. The direction of normal vector $\boldsymbol{n}$ is assumed to be pointing outward toward the continuous phase from the interface, and the direction of the tangent vector $\boldsymbol{t}$ is along the increasing value of the normalized arclength s. The interfacial viscosity traction $(\boldsymbol{f_\mu} + \boldsymbol{f_\kappa})$ is computed using Eqs. (5) and (6). We observe that the magnitude of the tangential component of the interfacial viscosity traction is much larger than the normal component along the thin film. We also observe that the traction around the films edges opposes the drainage of the fluid, while the traction in the films center region acts along the positive tangent direction and stretches the film. Overall, these effects reduce the pressure gradients in the thin film and widen the film. In Figs. 11(a) and 11(b), we also plot the tangential velocity along the film surface for shape profiles shown in Figs. 9(a) and 9(b), respectively. Upon comparing, we can see that the surface viscosity traction significantly reduces the film's tangential velocity compared to the clean droplet. Both a wider film and reduced drainage velocity contribute to the increased drainage time observed for droplets with surface viscosity. Lowered radial pressure gradients within a wider film for the droplet also inhibit shape dimpling, which is otherwise observed at high values of capillary number and large Marangoni numbers.

Next, we discuss the impact of surface viscosity on droplet coalescence at large capillary numbers $Ca \sim \mathcal{O}(10^{-2})$. At $Ca = 0.01$, Figs. 12(a) and 12(b) show the evolution of film shapes with drainage time for a clean droplet and a droplet with surface viscosity at $Bq = 0.1$. We see that the clean droplet reaches $h_{\min} = 2 \times 10^{-4}$ at $t_d = 3.1$, and the same minimum film thickness is reached for the droplet with surface viscosity at $t_d = 9.03$. When we compare the two shapes at the same height $h_{\min}$, we see that the lateral extent of the droplets are the same, but dimpling is less for the droplet with surface viscosity. This behavior is different from the observations discussed previously at $Ca = 0.0002$ and $Ca = 0.001$, where surface viscosity was found to simultaneously reduce dimpling and increase the lateral extent. At capillary number $Ca = 0.04$, Fig. 13 shows the film shape formed for a clean droplet ($Bq = 0$) and a droplet with surface viscosity ($Bq = 0.1$) at drainage times $t_d = 18.9$ and $t_d = 53.7$, respectively. Interestingly, a drainage profile similar to that of a clean droplet is

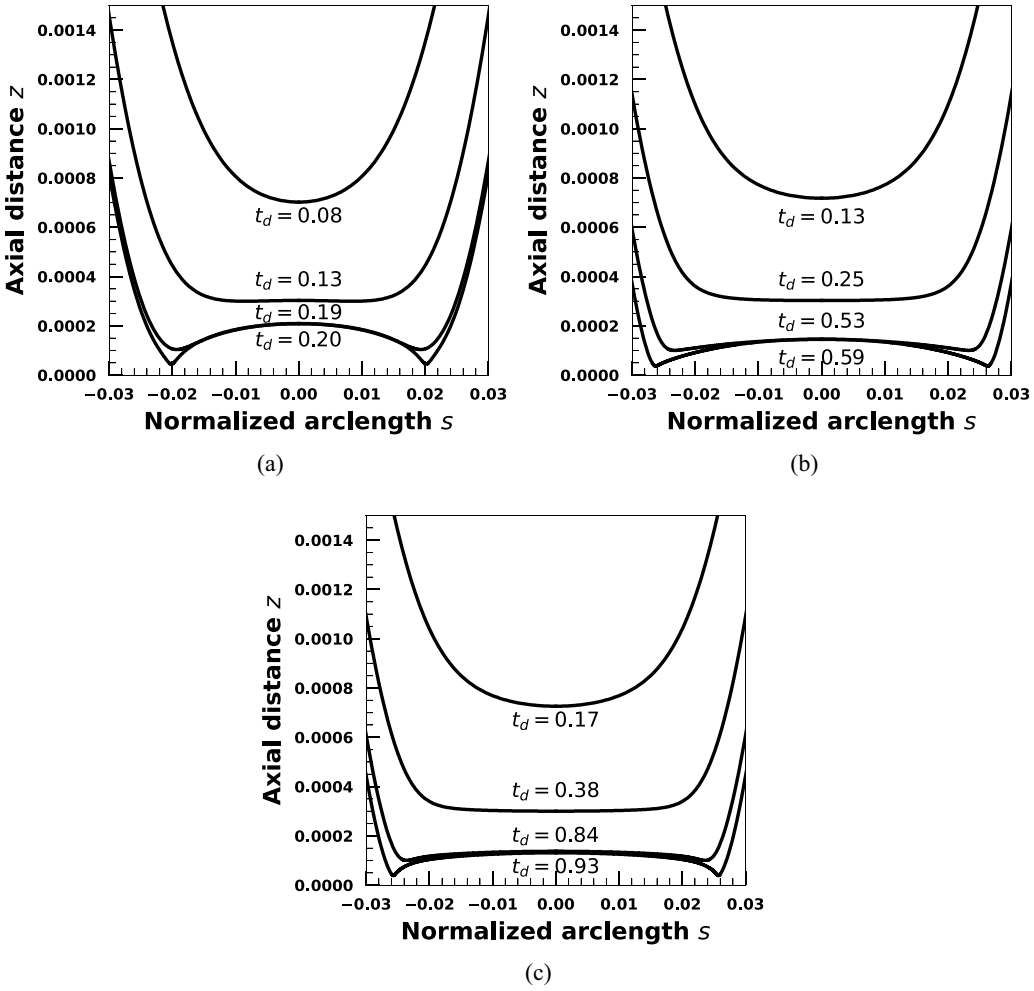

FIG. 9. Film drainage profiles for a clean droplet and droplets with surface viscosity at capillary number $Ca = 0.001$. (a) Clean droplet ($Bq = 0$), (b) Droplet with surface viscosity: $Bq = 0.1,\ \lambda_{ds} = 1$, and (c) Droplet with surface viscosity: $Bq = 0.2,\ \lambda_{ds} = 1$.

obtained for a droplet with surface viscosity but at a later drainage time t_d. Thus, at $Ca = 0.04$, surface viscosity increases the drainage time but does not alter the film dimpling and lateral extent of the dimpled region compared to a clean droplet. At even higher capillary number $Ca = 0.05$, Fig. 14 shows the evolution of film thickness h_{min} and h_{center} with drainage time t_d for a clean droplet $Bq = 0$ (red curves) and a droplet with surface viscosity $Bq = 0.1,\ \lambda_{ds} = 1$ (blue curves). We observe that both the clean droplet and the droplet with surface viscosity do not show coalescence and instead attain a steady droplet shape. It has been argued in the previous study on clean droplet coalescence that at very large capillary number values, the internal circulation inhibits the drainage process. As a result, the droplet system reaches a steady configuration, and coalescence is not observed [11].

Figure 15 shows how the total drainage time scaled by droplet radius ($T_d/R'^{5/4}\ \mu\text{m}^{-5/4}$) changes with the capillary number Ca for a clean droplet $Bq = 0$ (blue and red points) and droplet with surface viscosity at $Bq = 0.1$ (green points) and $Bq = 0.2$ (yellow points). It has been shown in previous literature on coalescence that for a droplet without surfactant ($Bq = 0$), the drainage time scales as $Ca^{4/3}$ at large values of capillary number when the thin film is significantly de-

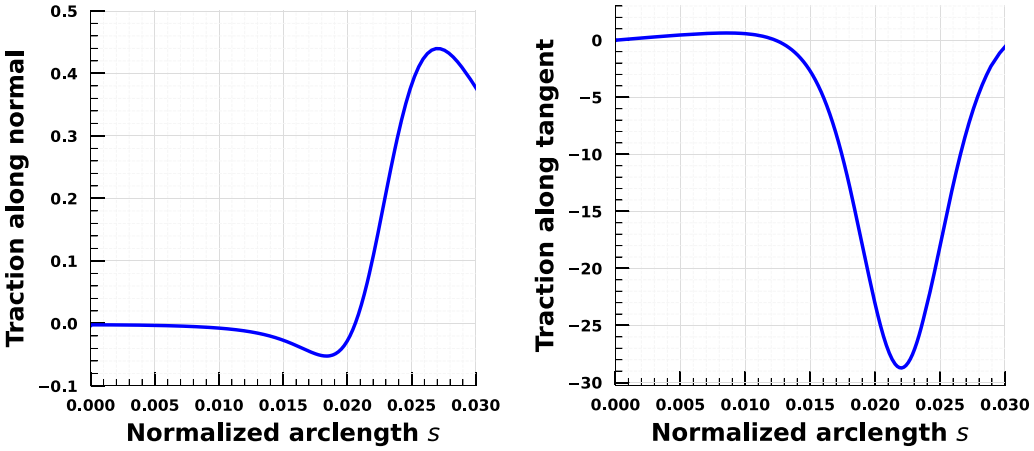

(a) (b)

FIG. 10. Normal and tangential component of the interfacial viscosity traction along the thin film corresponding to the droplet shape shown in 9(b) at drainage time $t_d = 0.25$. (a) Normal component of the interfacial viscosity traction. The direction of the normal vector is assumed to be pointing outward towards the continuous phase from the interface and (b) Tangential component of the interfacial viscosity traction. The direction of the tangent vector is along the increasing value of normalized arclength s.

formed/dimpled. This scaling is derived by assuming the thin film is flat and disklike near the point of contact [11,24]. However, at very small values of capillary number, it has been shown that drainage time scales as Ca^1 since the droplet is almost spherical near the point of contact [11,24]. In Fig. 15, the scaling of drainage time at large capillary number values is shown as $T_d \sim Ca^{4/3}$ using dashed lines, and at small capillary number values as $T_d \sim Ca$ by bold lines. We observe that surface viscosity increases the drainage time with respect to the clean droplet for the entire range

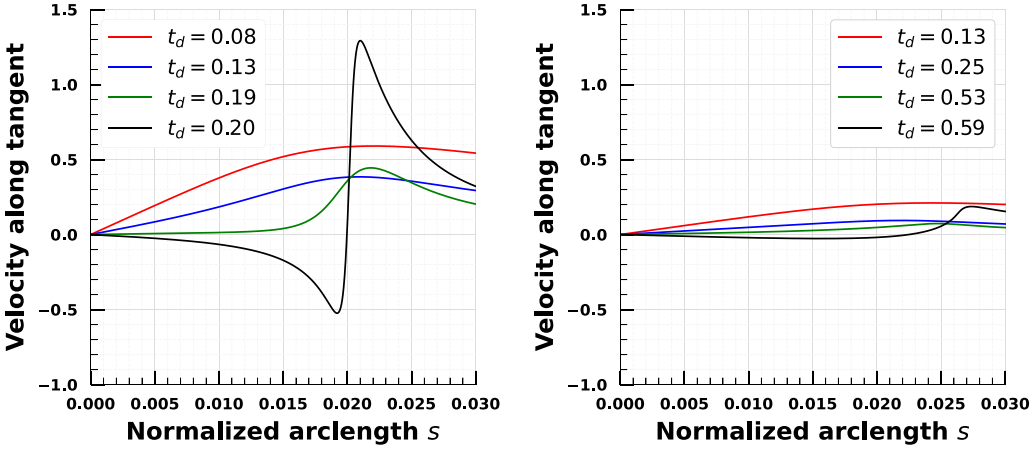

(a) (b)

FIG. 11. Tangential component of interfacial velocity computed along the thin film for film shapes shown in (a) Fig. 9(a), and (b) Fig. 9(b). (a) Droplet with $Bq = 0$ at $Ca = 0.001$. (b) Droplet with $Bq = 0.1$ at $Ca = 0.001$.

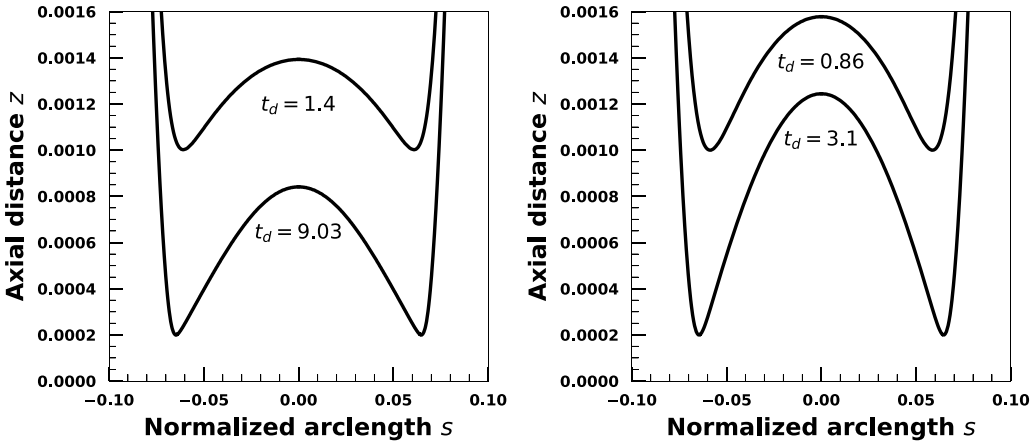

(a) (b)

FIG. 12. Film drainage profiles for clean droplet and a droplet with surface viscosity at $Ca = 0.01$ (a) Clean droplet ($Bq = 0$) and (b) Droplet with surface viscosity: $Bq = 0.1,\ \lambda_{ds} = 1$.

of capillary number $[\mathcal{O}(10^{-4}) - \mathcal{O}(10^{-2})]$, and scaling results similar to that of a clean droplet are observed at low and high values of capillary number.

C. Results: Droplet with constant surface viscosity and Marangoni flows

As the thin film drains, the surfactant gets swept toward the film's edges and gives rise to Marangoni stresses. The Marangoni stresses within the film enhance the film dimpling and increase the total drainage time compared to a clean droplet at the same capillary number. The effect of surfactant on droplet coalescence has been numerically studied in [24]. In the previous section, we saw the isolated impact of surface viscosity also increases the drainage time compared to a clean droplet at the same value of the capillary number. Unlike Marangoni stresses which increase the

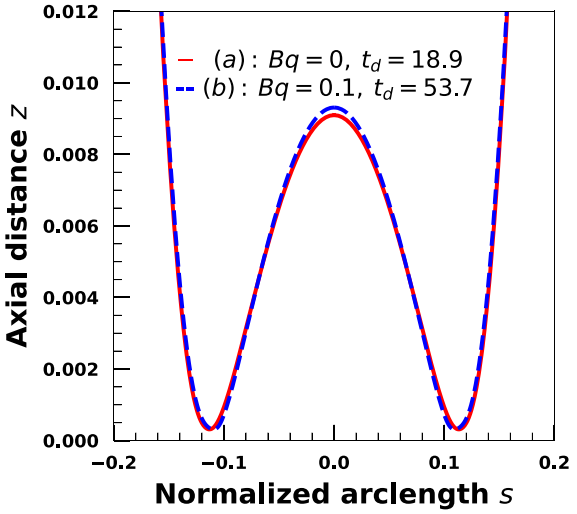

FIG. 13. Film drainage profiles at $Ca = 0.04$ for two cases: (a) Clean droplet $Bq = 0$ at drainage time $t_d = 18.9$ (red curve) and (b) Droplet with surface viscosity $Bq = 0.1,\ \lambda_{ds} = 1$ at drainage time $t_d = 53.7$ (blue curve).

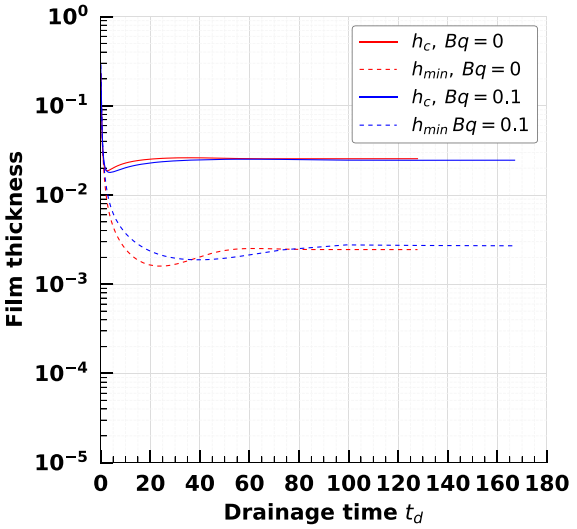

FIG. 14. Evolution of film thickness h_{min} and h_{center} with drainage time t_d at $Ca = 0.05$ for a clean droplet $Bq = 0$ (red curves) and a droplet with surface viscosity $Bq = 0.1$, $\lambda_{ds} = 1$ (blue curves).

dimpling of the film, surface viscosity appears to lessen the dimpling but widen the thin film. In this section, we discuss the coupling between surface viscosity effects and surfactant transport.

First, we look at a relatively low value of capillary number $Ca = 0.0002$. Figure 16(a) shows the film drainage profiles for a droplet with Marangoni effects ($Pe_s = 5.15$, $E = 0.25$) and without surface rheology. The total drainage time is $T_d = 0.25$, which is higher than that of a clean droplet [$T_d = 0.038$, see Fig. 7(a)] and a droplet with surface viscosity $Bq = 0.2$ and no surfactant transport [$T_d = 0.16$, see Fig. 7(b)]. Figure 16(b) shows the drainage profile for droplet with both surface viscosity $Bq = 0.2$ and surfactant transport ($Pe_s = 5.15$, $E = 0.25$). Relative to droplets with only

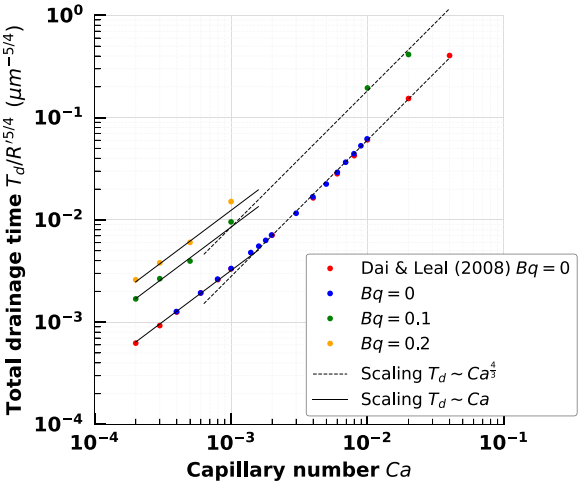

FIG. 15. Total drainage time scaled by droplet radius ($T_d/R'^{5/4}$ $\mu\text{m}^{-5/4}$) as a function of capillary number Ca for a clean droplet ($Bq = 0$, shown by blue points) and droplet with surface viscosity at $Bq = 0.1$ (shown by green points) and $Bq = 0.2$ (shown by yellow points). The scaling of drainage time at large capillary number values is shown as $T_d \sim Ca^{4/3}$ using dashed lines and at small capillary number values as $T_d \sim Ca$ by bold lines.

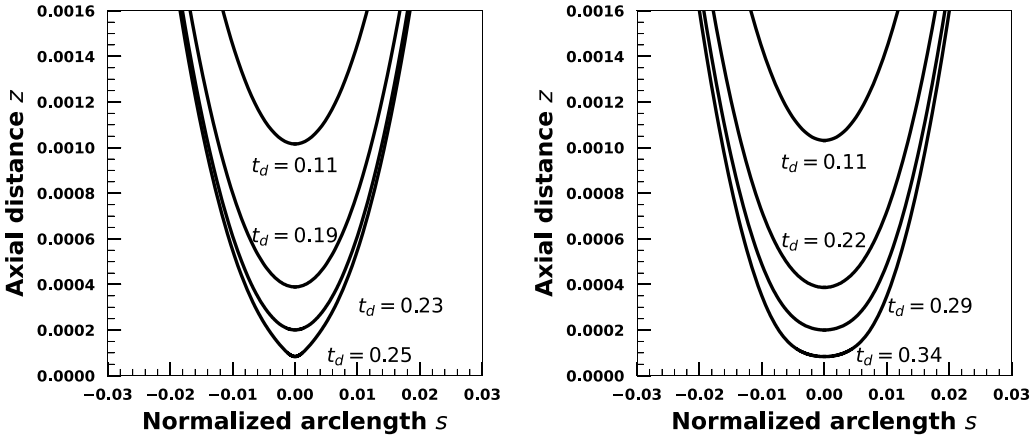

(a) (b)

FIG. 16. Film drainage profiles for a droplet with Marangoni effects. The dimensionless parameters are $Ca = 0.0002$, $E = 0.25$, and $Pe_s = 5.15$. (a) Droplet without surface viscosity $Bq = 0$ and (b) Droplet with surface viscosity $Bq = 0.2$.

surfactant transport, we observe that a droplet with both surface viscosity and surfactant transport form a wider film and has higher drainage time $T_d = 0.34$. No dimpling is observed at this value of capillary number.

Next, we will look at capillary number $Ca = 0.001$. In the previous section, we observed that at $Ca = 0.001$, the drainage time for a clean droplet is $T_d = 0.20$ [see Fig. 9(a)], while the drainage time for a droplet with surface viscosity $Bq = 0.1$ and without surfactant transport is $T_d = 0.59$ [see Fig. 9(b)]. Figure 17(a) shows the film drainage profiles for a droplet with surfactant transport and without surface viscosity ($Pe_s = 25.7$, $E = 0.25$, $Bq = 0$). We observe that Marangoni stresses enhance the dimpling of the film and increase the drainage time relative to droplet shapes shown in Figs. 9(b) and 9(a). Figure 17(b) shows the combined effect of surface viscosity and surfactant

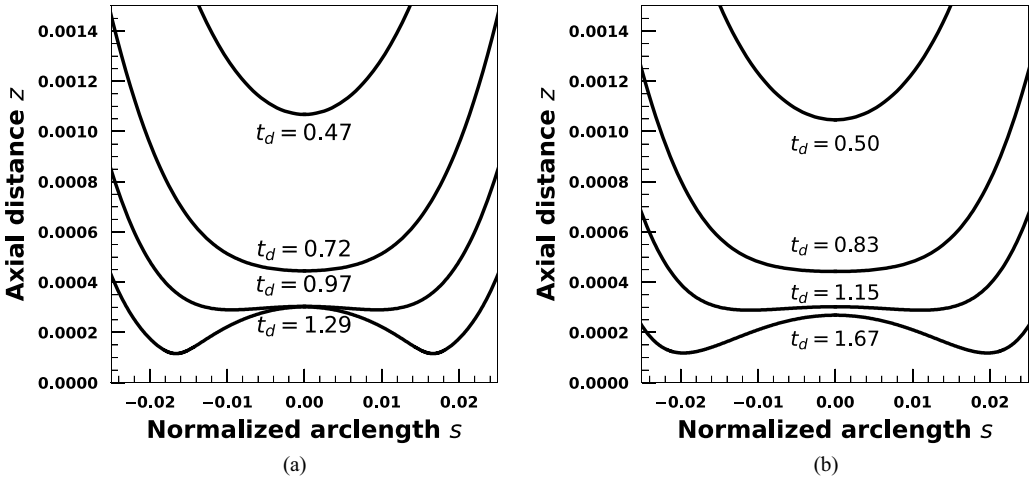

(a) (b)

FIG. 17. Film drainage profiles for a droplet with Marangoni effects. The dimensionless parameters are $Ca = 0.001$, $E = 0.25$, and $Pe_s = 25.7$. (a) Droplet without surface viscosity $Bq = 0$ and (b) Droplet with surface viscosity $Bq = 0.1$.

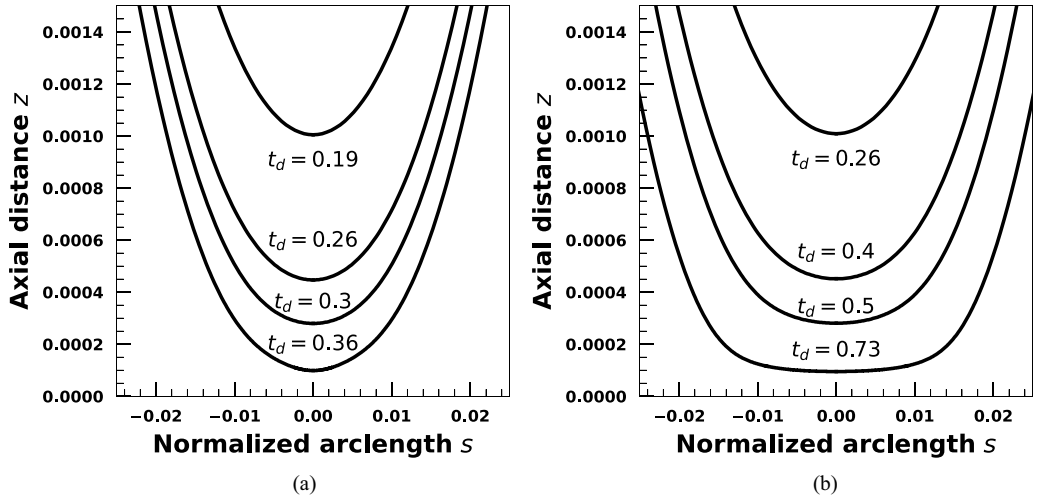

FIG. 18. Film drainage profiles for a droplet with Marangoni effects. The dimensionless parameters are $Ca = 0.001$, $E = 0.1$, and $Pe_s = 25.7$. (a) Droplet without surface viscosity $Bq = 0$ and (b) Droplet with surface viscosity $Bq = 0.1$.

transport ($Pe_s = 25.7$, $E = 0.25$, $Bq = 0.1$). Unlike a droplet with only surface viscosity, which appears to form a flat film, the droplet with both surface viscosity and surfactant transport forms a dimpled film. Upon comparing Figs. 17(a) and 17(b), we see that surface viscosity widens the film and lessens the film dimpling. The combined effect of surface viscosity and surfactant transport also increases the drainage time compared to a droplet with only surfactant transport.

In Fig. 18, we reduce the surface elasticity number and plot the drainage profiles at $E = 0.1$, $Pe = 25.7$, and $Ca = 0.001$ for a droplet with and without surface viscosity [Figs. 18(a) and 18(b), respectively]. We find that surface viscosity flattens the film and increases the drainage time at $E = 0.1$. Upon comparing Fig. 18 with Fig. 17, we find that the impact of surface viscosity on drainage time is more significant at $E = 0.1$. We note that as the surface elasticity/surface Peclet number increases, the Marangoni effects become more important compared to surface viscosity effects.

D. Results: Droplet with pressure-dependent surface viscosity and Marangoni flows

In the previous section, we assumed the surface viscosity remains constant on the interface. Generally, surface viscosity does not remain constant and can vary strongly with surface pressure. In the following discussion, we assume an exponential dependence of surface viscosity on surface pressure:

$$Bq^{\pm} = Bq_{\text{eq}}\, e^{\pm \frac{1-\sigma}{\Pi_C}}. \tag{16}$$

Figure 19 shows the drainage profiles for a droplet with surface viscosity $Bq = 0.2$ at $Ca = 0.0002$ for two cases: (a) pressure-thickening surfactant $\Pi_C = 0.1$, and (b) pressure-thinning surfactant $\Pi_C = 0.1$. The surfactant parameters are $Pe_s = 5.15$, $E = 0.25$. As we can see, the results for a pressure-thickening surfactant overlap with the results for a pressure-thinning surfactant. The drainage time is the same as that of a droplet with a pressure-independent surfactant.

In Fig. 20 we plot the effect of pressure thickening and thinning surfactants on drainage profiles at $Ca = 0.001$, $Pe_s = 25.75$, $Bq = 0.1$, and $E = 0.25$. We see that, even at a higher value of capillary number $Ca = 0.001$ with dimpling effects, the results for a pressure thickening and a pressure-thinning surfactant overlap.

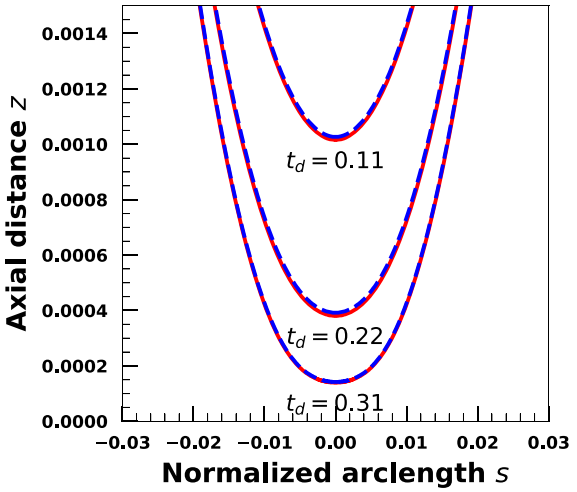

FIG. 19. Film drainage profiles for a droplet with pressure-dependent surface viscosity at $Ca = 0.0002$ and $Bq = 0.2$. Blue curves represent results for pressure-thinning surfactant $\Pi_C = 0.1$, and red curves represent results for pressure-thickening surfactant $\Pi_C = 0.1$. Surfactant parameters are: $Pe_s = 5.15$, $E = 0.25$.

For the surfactant parameter values considered in this work, the effect of pressure-thinning/thickening surfactant does not change coalescence dynamics. We note that in this work, the equilibrium surface coverage is dilute (as described in experiment [11]), and the Boussinesq number values are small. The dilute equilibrium surfactant concentration leads to a small decrease/increase in Bq that does not change the coalescence dynamics significantly compared to a pressure-independent surfactant.

For larger equilibrium surfactant concentrations, both the Marangoni effects and the variation in Bq from its equilibrium value for pressure thickening and thinning surfactants will increase.

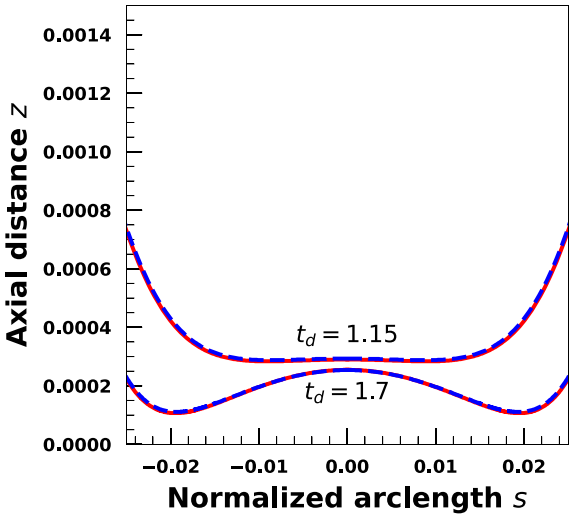

FIG. 20. Film drainage profiles for a droplet with pressure-dependent surface viscosity at $Ca = 0.001$ and $Bq = 0.1$. Blue curves represent results for pressure-thickening surfactant $\Pi_C = 0.1$, and red curves represent results for pressure-thinning surfactant $\Pi_C = 0.1$. Surfactant parameters are: $Pe_s = 25.75$, $E = 0.25$.

For stronger Marangoni stresses, the surface rheology effects can become less important, and it is unclear whether the combined influence would show different behavior for pressure thinning/thickening surfactants. We will not comment on this point further and leave it for a future manuscript.

IV. CONCLUSION AND FUTURE WORK

In this work, we explore how the surface rheology of adsorbed viscous surfactants alters droplet coalescence. We develop axisymmetric boundary-integral simulations to model the full coalescence process from the approach of two equal sized spherical droplets under uniaxial compressional flow to the eventual formation and drainage of the thin film formed between the two droplets. We model the viscous droplet interface using the Boussinesq-Scriven constitutive relationship. We assume the adsorbed surfactant is insoluble and incorporate the effect of surfactant transport using the convection-diffusion equation. We assume the Langmuir equation of state to correlate interfacial tension with surfactant concentration changes.

We examine the role of interfacial viscosity on film profiles and drainage time. We find that the film drainage behavior of a droplet with surface viscosity is not altered by the relative ratio of shear to dilatational viscosity but rather depends on the sum of shear and dilatational Boussinesq numbers. This is in contrast to the effect of surface viscosity on droplet breakup in a linear flow field and droplet instabilities during sedimentation. For these processes, surface shear viscosity is found to reduce droplet deformation and increase the critical capillary number, while surface dilatational viscosity is found to have the opposite effect (i.e., increase deformation and reduce the critical capillary number) [61,63–65].

In droplet coalescence, the interfacial traction significantly reduces the film's drainage velocity compared to a clean droplet. As a result, surface viscosity substantially slows down the film drainage. At $Bq = 0.1$, we observe that the total film drainage time increases by roughly the same scale factor relative to a clean droplet for the capillary number in the range $\mathcal{O}(10^{-4})$–$\mathcal{O}(10^{-2})$. However, the impact of surface viscosity on the film profiles differs at each capillary number order.

(i) At a low capillary number value $Ca = 2 \cdot 10^{-4}$, for a clean droplet, the shape of the thin film remains spherical as the film drains, and rupture occurs at the center of the droplet. However, in the case of a droplet with surface viscosity, we observe that the droplet develops a relatively flatter film, and at a sufficiently high value of Boussinesq number $Bq = 0.2$, the rupture occurs at the edges of the planar center region.

(ii) At a moderate value of capillary number $Ca = 10^{-3}$, a clean droplet develops a dimpled shape. For a droplet with surface viscosity, we observe that the surface viscosity flattens and widens the film and reduces the film dimpling compared to a clean droplet.

(iii) At large capillary numbers $Ca = \mathcal{O}(10^{-2})$, a clean droplet forms a highly dimpled film. We observe that, at this order of capillary number, surface viscosity does not alter the lateral extent of the dimpled region compared to the clean droplet. The influence of surface viscosity on film dimpling also decreases as the capillary number increases in this range. At $Ca = 4 \cdot 10^{-2}$, for a droplet with surface viscosity, the drainage profiles are similar to that observed for a clean droplet, even though we observe a higher total film drainage time than a clean droplet. And at $Ca = 5 \cdot 10^{-2}$, we find that both a clean droplet and a droplet with surface viscosity ($Bq = 0.1$) do not coalesce. At this capillary number, the droplet system attains a steady configuration under flow.

Lastly, it is well known that at moderate values of capillary number, surfactant transport delays the coalescence by increasing the dimpling of the film. This stabilization mechanism differs from surface viscosity, which delays drainage by reducing dimpling and widening the film. We performed simulations to find the combined effect of surface viscosity and Marangoni stresses. We find that including both effects increases the drainage time compared to a droplet with only surfactant transport. The film formed is less dimpled and wider than the droplet without surface viscosity and with surfactant transport. We also discuss the impact of pressure thickening/thinning surfactant on film drainage. Pressure thickening and thinning surfactants have been shown to alter droplet breakup

and sedimentation in previous studies [61,64], but for droplet coalescence, we observe that the film drainage is not altered by pressure-thickening/thinning surfactants and results are the same as that of a pressure-independent surfactant. This is because, during coalescence, the change in surface pressure along the film is not large enough to exhibit significant changes in Boussinesq numbers.

In this study, we assume an axisymmetric geometry and that the collision between the two droplets is head-on. However, in real systems, it is difficult to achieve a head-on collision. Even small ambient disturbances can cause offsets from the inflow axes of the flow leading to glancing collisions. Since the extension felt by the droplet is time dependent in glancing collisions, a finite time is available for coalescence to occur before the pair of droplets rotate and move apart. Therefore, a critical capillary number is observed below which the coalescence occurs. For glancing collision, it has been shown in previous literature that the critical capillary number for coalescence reduces with increasing the initial offset. The results from this work can provide an approximate analysis in situations where either the offset from the inflow axes of the flow is very small, or the capillary number is very low, as this has also been the case with clean droplets and droplets with surfactant transport [11,24].

In this work, we also assume the adsorbed surfactant is insoluble and viscous. In the future, it will be important to include the effect of surfactant elasticity in our numerical simulations to examine its role in the drainage between two droplets undergoing coalescence for generalized surface-active agents [66]. In a future publication, we would also like to include the effects of surfactant solubility in the limit of kinetically limited adsorption/desorption.

ACKNOWLEDGMENT

The authors would like to thank the Michael and Carolyn Ott Endowment of Purdue University.

[1] S. Schütz, G. Gorbach, and M. Piesche, Modeling fluid behavior and droplet interactions during liquid–liquid separation in hydrocyclones, Chem. Eng. Sci. **64**, 3935 (2009).

[2] M. Kumar, R. S. Bishnoi, A. K. Shukla, and C. P. Jain, Techniques for formulation of nanoemulsion drug delivery system: A review, Prev. Nutr. Food Sci. **24**, 225 (2019).

[3] A. Ammala, Biodegradable polymers as encapsulation materials for cosmetics and personal care markets, Int. J. Cos. Sci. **35**, 113 (2013).

[4] D. Pradilla, S. Simon, J. Sjoblom, J. Samaniuk, M. Skrzypiec, and J. Vermant, Sorption and interfacial rheology study of model asphaltene compounds, Langmuir **32**, 2900 (2016).

[5] R. Daly, T. S. Harrington, G. D. Martin, and I. M. Hutchings, Inkjet printing for pharmaceutics–a review of research and manufacturing, Int. J. Pharma. **494**, 554 (2015).

[6] B. He, S. Yang, Z. Qin, B. Wen, and C. Zhang, The roles of wettability and surface tension in droplet formation during inkjet printing, Sci. Rep. **7**, 1 (2017).

[7] Y. Behjat, S. Shahhosseini, and M. A. Marvast, Modeling gas oil spray coalescence and vaporization in gas solid riser reactor, Int. Commun. Heat Mass Transfer **37**, 935 (2010).

[8] Z. Mahmood, M. Jahangir, M. Liaquat, S. W. Ahmad Shah, M. Mumtaz Khan, R. Stanley, and B. D'Arcy, Potential of nano-emulsions as phytochemical delivery system for food preservation, Pakistan Journal of Pharmaceutical Sciences **30**, 2259 (2017).

[9] C. Berton-Carabin and K. Schroën, Towards new food emulsions: Designing the interface and beyond, Current Opinion in Food Science **27**, 74 (2019).

[10] A. K. Chesters, Modelling of coalescence processes in fluid-liquid dispersions: a review of current understanding, Chem. Eng. Res. Design **69**, 259 (1991).

[11] Y. Yoon, F. Baldessari, H. D. Ceniceros, and L. G. Leal, Coalescence of two equal-sized deformable drops in an axisymmetric flow, Phys. Fluids **19**, 102102 (2007).

[12] H. Yang, C. C. Park, Y. T. Hu, and L. G. Leal, The coalescence of two equal-sized drops in a two-dimensional linear flow, Phys. Fluids **13**, 1087 (2001).
[13] I. B. Ivanov, K. D. Danov, and P. A. Kralchevsky, Flocculation and coalescence of micron-size emulsion droplets, Colloids Surf., A **152**, 161 (1999).
[14] S. G. Yiantsios and R. H. Davis, On the buoyancy-driven motion of a drop towards a rigid surface or a deformable interface, J. Fluid Mech. **217**, 547 (1990).
[15] S. G. Yiantsios and R. H. Davis, Close approach and deformation of two viscous drops due to gravity and van der waals forces, J. Colloid Interface Sci. **144**, 412 (1991).
[16] D. Li, Coalescence between two small bubbles or drops, J. Colloid Interface Sci. **163**, 108 (1994).
[17] D. S. Valkovska, K. D. Danov, and I. B. Ivanov, Effect of surfactants on the stability of films between two colliding small bubbles, Colloids Surf. A **175**, 179 (2000).
[18] L. Y. Yeo, O. K. Matar, E. S. P. de Ortiz, and G. F. Hewitt, Film drainage between two surfactant-coated drops colliding at constant approach velocity, J. Colloid Interface Sci. **257**, 93 (2003).
[19] V. Cristini, J. Bławzdziewicz, and M. Loewenberg, An adaptive mesh algorithm for evolving surfaces: simulations of drop breakup and coalescence, J. Comput. Phys. **168**, 445 (2001).
[20] P. Janssen, P. Anderson, G. Peters, and H. Meijer, Axisymmetric boundary integral simulations of film drainage between two viscous drops, J. Fluid Mech. **567**, 65 (2006).
[21] A. K. Chesters and I. B. Bazhlekov, Effect of insoluble surfactants on drainage and rupture of a film between drops interacting under a constant force, J. Colloid Interface Sci. **230**, 229 (2000).
[22] V. Cristini, J. Bławzdziewicz, and M. Loewenberg, Near-contact motion of surfactant-covered spherical drops, J. Fluid Mech. **366**, 259 (1998).
[23] Y. Yoon, A. Hsu, and L. G. Leal, Experimental investigation of the effects of copolymer surfactants on flow-induced coalescence of drops, Phys. Fluids **19**, 023102 (2007).
[24] B. Dai and L. G. Leal, The mechanism of surfactant effects on drop coalescence, Phys. Fluids **20**, 040802 (2008).
[25] C. Vannozzi, Coalescence of surfactant covered drops in extensional flows: effects of the interfacial diffusivity, Phys. Fluids **24**, 082101 (2012).
[26] S. Narayan, A. E. Metaxas, R. Bachnak, T. Neumiller, and C. S. Dutcher, Zooming in on the role of surfactants in droplet coalescence at the macroscale and microscale, Curr. Opin. Colloid Interface Sci. **50**, 101385 (2020).
[27] R. E. Kurtz, A. Lange, and G. G. Fuller, Interfacial rheology and structure of straight-chain and branched fatty alcohol mixtures, Langmuir **22**, 5321 (2006).
[28] C. F. Brooks, G. G. Fuller, C. W. Frank, and C. R. Robertson, An interfacial stress rheometer to study rheological transitions in monolayers at the air-water interface, Langmuir **15**, 2450 (1999).
[29] K. S. Yim and G. G. Fuller, Influence of phase transition and photoisomerization on interfacial rheology, Phys. Rev. E **67**, 041601 (2003).
[30] R. Ghaskadvi, J. B. Ketterson, R. MacDonald, and P. Dutta, Apparatus to measure the shear modulus of langmuir monolayers as functions of strain amplitude and frequency, Rev. Sci. Instrum. **68**, 1792 (1997).
[31] D. Barthes-Biesel, Motion and deformation of elastic capsules and vesicles in flow, Annu. Rev. Fluid Mech. **48**, 25 (2016).
[32] P. M. Vlahovska and R. S. Gracia, Dynamics of a viscous vesicle in linear flows, Phys. Rev. E **75**, 016313 (2007).
[33] P. Cicuta, Compression and shear surface rheology in spread layers of β-casein and β-lactoglobulin, J. Colloid Interface Sci. **308**, 93 (2007).
[34] M. Pepicelli, T. Verwijlen, T. A. Tervoort, and J. Vermant, Characterization and modelling of langmuir interfaces with finite elasticity, Soft Matter **13**, 5977 (2017).
[35] T. Verwijlen, P. Moldenaers, and J. Vermant, A fixture for interfacial dilatational rheometry using a rotational rheometer, Eur. Phys. J.: Spec. Top. **222**, 83 (2013).
[36] G. G. Fuller and J. Vermant, Complex fluid-fluid interfaces: rheology and structure, Ann. Rev. Chem. Biomol. Eng. **3**, 519 (2012).

[37] A. P. Gunning, A. R. Kirby, P. J. Wilde, R. Penfold, N. C. Woodward, and V. J. Morris, Probing the role of interfacial rheology in the relaxation behaviour between deformable oil droplets using force spectroscopy, Soft Matter **9**, 11473 (2013).
[38] M. J. Boussinesq, Sur l'existence d'une viscosité superficielle, dans la mince couche de transition séparant un liquide d'un autre fluide contigu, Ann. Chim. Phys. **29**, 349 (1913).
[39] L. Scriven, Dynamics of a fluid interface equation of motion for newtonian surface fluids, Chem. Eng. Sci. **12**, 98 (1960).
[40] H. Stone, A simple derivation of the time-dependent convective-diffusion equation for surfactant transport along a deforming interface, Phys. Fluids **2**, 111 (1990).
[41] H. Wong, D. Rumschitzki, and C. Maldarelli, On the surfactant mass balance at a deforming fluid interface, Phys. Fluids **8**, 3203 (1996).
[42] J. R. Samaniuk and J. Vermant, Micro and macrorheology at fluid–fluid interfaces, Soft Matter **10**, 7023 (2014).
[43] K. Kim, S. Q. Choi, J. A. Zasadzinski, and T. M. Squires, Interfacial microrheology of dppc monolayers at the air–water interface, Soft Matter **7**, 7782 (2011).
[44] K. Kim, S. Q. Choi, Z. A. Zell, T. M. Squires, and J. A. Zasadzinski, Effect of cholesterol nanodomains on monolayer morphology and dynamics, Proc. Natl. Acad. Sci. USA **110**, E3054 (2013).
[45] Z. A. Zell, A. Nowbahar, V. Mansard, L. G. Leal, S. S. Deshmukh, J. M. Mecca, C. J. Tucker, and T. M. Squires, Surface shear inviscidity of soluble surfactants, Proc. Natl. Acad. Sci. USA **111**, 3677 (2014).
[46] A. Ponce-Torres, M. Rubio, M. Herrada, J. Eggers, and J. Montanero, Influence of the surface viscous stress on the pinch-off of free surfaces loaded with nearly-inviscid surfactants, Sci. Rep. **10**, 16065 (2020).
[47] E. M. Freer, K. S. Yim, G. G. Fuller, and C. J. Radke, Interfacial rheology of globular and flexible proteins at the hexadecane/water interface: comparison of shear and dilatation deformation, J. Phys. Chem. B **108**, 3835 (2004).
[48] E. Hildebrandt, H. Nirschl, R. J. Kok, and G. Leneweit, Adsorption of phospholipids at oil/water interfaces during emulsification is controlled by stress relaxation and diffusion, Soft Matter **14**, 3730 (2018).
[49] G. Espinosa, I. López-Montero, F. Monroy, and D. Langevin, Shear rheology of lipid monolayers and insights on membrane fluidity, Proc. Natl. Acad. Sci. USA **108**, 6008 (2011).
[50] J. Krägel, G. Kretzschmar, J. Li, G. Loglio, R. Miller, and H. Möhwald, Surface rheology of monolayers, Thin Solid Films **284-285**, 361 (1996).
[51] P. Erni, E. J. Windhab, and P. Fischer, Emulsion drops with complex interfaces: Globular versus flexible proteins, Macromol. Mater. Eng. **296**, 249 (2011).
[52] E. M. Freer, K. S. Yim, G. G. Fuller, and C. J. Radke, Shear and dilatational relaxation mechanisms of globular and flexible proteins at the hexadecane/water interface, Langmuir **20**, 10159 (2004).
[53] W. Xiong, C. Ren, M. Tian, X. Yang, J. Li, and B. Li, Emulsion stability and dilatational viscoelasticity of ovalbumin/chitosan complexes at the oil-in-water interface, Food Chem. **252**, 181 (2018).
[54] P. Erni, P. Fischer, E. J. Windhab, V. Kusnezov, H. Stettin, and J. Läuger, Stress-and strain-controlled measurements of interfacial shear viscosity and viscoelasticity at liquid/liquid and gas/liquid interfaces, Rev. Sci. Instrum. **74**, 4916 (2003).
[55] S. Narayan, I. Makhnenko, D. B. Moravec, B. G. Hauser, A. J. Dallas, and C. S. Dutcher, Insights into the microscale coalescence behavior of surfactant-stabilized droplets using a microfluidic hydrodynamic trap, Langmuir **36**, 9827 (2020).
[56] A. Shmyrov and A. Mizev, Surface diffusion in gaseous monolayers of an insoluble surfactant, Langmuir **35**, 14180 (2019).
[57] E. Hermans and J. Vermant, Interfacial shear rheology of dppc under physiologically relevant conditions, Soft Matter **10**, 175 (2014).
[58] G. T. Gavranovic, R. E. Kurtz, K. Golemanov, A. Lange, and G. G. Fuller, Interfacial rheology and structure of straight-chain and branched hexadecanol mixtures, Ind. Eng. Chem. Res. **45**, 6880 (2006).
[59] C. Pozrikidis, The instability of a moving viscous drop, J. Fluid Mech. **210**, 1 (1990).
[60] C. Pozrikidis *et al.*, *Boundary Integral and Singularity Methods for Linearized Viscous Flow* (Cambridge University Press, New York, NY, 1992).

[61] N. Singh and V. Narsimhan, Impact of surface viscosity on the stability of a droplet translating through a stagnant fluid, J. Fluid Mech. **927**, A44 (2021).
[62] E. Chatzigiannakis, N. Jaensson, and J. Vermant, Thin liquid films: Where hydrodynamics, capillarity, surface stresses and intermolecular forces meet, Curr. Opin. Colloid Interface Sci. **53**, 101441 (2021).
[63] N. Singh and V. Narsimhan, Deformation and burst of a liquid droplet with viscous surface moduli in a linear flow field, Phys. Rev. Fluids **5**, 063601 (2020).
[64] N. Singh and V. Narsimhan, Numerical investigation of the effect of surface viscosity on droplet breakup and relaxation under axisymmetric extensional flow, J. Fluid Mech. **946**, A24 (2022).
[65] V. Narsimhan, Shape and rheology of droplets with viscous surface moduli, J. Fluid Mech. **862**, 385 (2019).
[66] A. Ramachandran and G. Leal, A scaling theory for the hydrodynamic interaction between a pair of vesicles or capsules, Phys. Fluids **22**, 091702 (2010).